

Numerical study of the influence of turbulence-chemistry interaction in URANS simulations of diesel spray flame structures under marine engine-like conditions

Ong, Jiun Cai ; Pang, Kar Mun ; Jangi, Mehdi; Bai, Xue-Song; Walther, Jens Honore

DOI:

[10.1021/acs.energyfuels.1c01091](https://doi.org/10.1021/acs.energyfuels.1c01091)

License:

None: All rights reserved

Document Version

Peer reviewed version

Citation for published version (Harvard):

Ong, JC, Pang, KM, Jangi, M, Bai, X-S & Walther, JH 2021, 'Numerical study of the influence of turbulence-chemistry interaction in URANS simulations of diesel spray flame structures under marine engine-like conditions', *Energy & Fuels*, vol. 35, no. 14, pp. 11457-11467. <https://doi.org/10.1021/acs.energyfuels.1c01091>

[Link to publication on Research at Birmingham portal](#)

Publisher Rights Statement:

This document is the Accepted Manuscript version of a Published Work that appeared in final form in *Energy and Fuels*, copyright © American Chemical Society after peer review and technical editing by the publisher. To access the final edited and published work see <https://doi.org/10.1021/acs.energyfuels.1c01091>

General rights

Unless a licence is specified above, all rights (including copyright and moral rights) in this document are retained by the authors and/or the copyright holders. The express permission of the copyright holder must be obtained for any use of this material other than for purposes permitted by law.

- Users may freely distribute the URL that is used to identify this publication.
- Users may download and/or print one copy of the publication from the University of Birmingham research portal for the purpose of private study or non-commercial research.
- User may use extracts from the document in line with the concept of 'fair dealing' under the Copyright, Designs and Patents Act 1988 (?)
- Users may not further distribute the material nor use it for the purposes of commercial gain.

Where a licence is displayed above, please note the terms and conditions of the licence govern your use of this document.

When citing, please reference the published version.

Take down policy

While the University of Birmingham exercises care and attention in making items available there are rare occasions when an item has been uploaded in error or has been deemed to be commercially or otherwise sensitive.

If you believe that this is the case for this document, please contact UBIRA@lists.bham.ac.uk providing details and we will remove access to the work immediately and investigate.

This document is confidential and is proprietary to the American Chemical Society and its authors. Do not copy or disclose without written permission. If you have received this item in error, notify the sender and delete all copies.

**Numerical Study of the Influence of Turbulence-Chemistry
Interaction in URANS Simulations of Diesel Spray Flame
Structures under Marine Engine-Like Conditions**

| | |
|-------------------------------|-------------------------------------------------------------------------------------------------------------------------------------------------------------------------------------------------------------------------------------------------------------------------------------------------------------------------------|
| Journal: | <i>Energy & Fuels</i> |
| Manuscript ID | ef-2021-01091j.R2 |
| Manuscript Type: | Article |
| Date Submitted by the Author: | n/a |
| Complete List of Authors: | Ong, Jiun Cai; Technical University of Denmark, Mechanical Engineering Pang, Kar Mun; MAN Energy Solutions Jangi, Mehdi; University of Birmingham, Mechanical Engineering Bai, Xue-Song; Lund Institute of Technology, Lund University, Dept. of Energy Sciences Walther, Jens; Danmarks Tekniske Universitet, |
| | |

SCHOLARONE™
Manuscripts

1
2
3
4
5
6
7 Numerical Study of the Influence of Turbulence-
8
9
10
11 Chemistry Interaction in URANS Simulations of
12
13
14
15 Diesel Spray Flame Structures under Marine Engine-
16
17
18
19 Like Conditions
20
21
22
23
24

25 *Jiun Cai Ong^{a*}, Kar Mun Pang^b, Mehdi Jangr^c, Xue-Song Bai^d, Jens Honore Walther^{a,e}*
26
27
28

29 ^a Department of Mechanical Engineering, Technical University of Denmark, 2800 Kgs. Lyngby,
30
31
32
33 Denmark
34
35

36 ^b MAN Energy Solutions, Teglholmsgade 41, 2450 København SV, Denmark
37
38

39 ^c Department of Mechanical Engineering, University of Birmingham, B15 2TT Birmingham, UK
40
41

42 ^d Department of Energy Sciences, Lund University, 22100 Lund, Sweden
43
44

45
46 ^e Computational Science and Engineering Laboratory, ETH Zürich, CH-8092 Zürich,
47
48
49 Switzerland
50
51

52
53 **KEYWORDS**
54

55
56 Ambient density, Eulerian Stochastic Fields, Nozzle diameter, Spray flame, Marine engine
57
58
59

ABSTRACT

The present work performs Unsteady Reynolds-averaged Navier-Stokes simulations to study the effect of turbulence-chemistry interaction (TCI) on diesel spray flames. Three nozzle diameters (d_0) of 100 μm , 180 μm , and 363 μm are considered in the present study. The Eulerian Stochastic Fields (ESF) method (with TCI effect) and Well-Stirred Reactor (WSR) model (without TCI effect) are considered in the present work. The model evaluation is carried out for ambient gas densities (ρ_{am}) of 30.0 kg/m^3 and 58.5 kg/m^3 . ESF method is demonstrated to be able to reproduce the ignition delay time (IDT), and lift-off length (LOL) with an improved accuracy than that from the WSR method. Furthermore, TCI has relatively more influence on LOL than on IDT. A normalized LOL (LOL*) is introduced, which considers the effect of d_0 , and its subsequent effect on the fuel-richness in the rich premixed core region is analyzed. The RO_2 distribution is less influenced by the TCI effect as ambient density increases. The ESF model generally predicts longer and wider CH_2O distribution. The difference in the spatial distribution of CH_2O between the ESF and WSR model diminishes as d_0 increases. At $\rho_{am} = 30.0 \text{ kg/m}^3$, the ESF method results in a broader region of OH with a lower peak OH values than in the WSR case. However, at $\rho_{am} = 58.5 \text{ kg/m}^3$, the variation of peak OH value is less susceptible to the increase in d_0 and the presence of TCI model. Furthermore, the influence of the TCI on the total OH mass decreases as d_0 increases. The total NO_x mass qualitatively follows the same trend as the total OH mass. This present work clearly shows that influence of TCI on the global spray and combustion characteristics becomes less prominent when d_0 increases.

1. INTRODUCTION

Diesel engines are and will remain in any foreseeable future the dominant propulsion system for maritime industries. With the aim to reduce emissions of greenhouse gases and pollutants, the maritime industry focuses on the use of alternative fuels in recent years⁽¹⁾. These alternative fuels have to be ignited with a small amount of directly injected conventional diesel fuel, commonly referred to as a “pilot fuel injection”. Ignition delay time (IDT), ignition location and the subsequent flame development of the pilot fuel are crucial to efficiently burn the succeeding alternative fuels delivered during the main injection event. In these engines, the in-cylinder pressure (or ambient density, ρ_{am}) at the time when pilot fuel is delivered varies significantly with engine loads⁽²⁾. Both numerical and experimental studies performed in an optical accessible constant volume combustion chamber (CVCC) under diesel engine-like conditions have shown that the flame size at quasi-steady state is reduced for increasing ρ_{am} ^(3,4). A pilot spray flame that is small and narrow can only increase the in-cylinder temperature locally and hence not optimum for igniting the main fuel. In other optical measurements, the quasi-steady state flame size is shown to increase with increasing nozzle diameter (d_0)⁽³⁾. This was found to increase the in-cylinder temperature in a larger region, which is expected to result in a better ignition of the main fuel. However, increasing d_0 can lead to negative consequences, e.g. larger amount of soot formed⁽⁴⁾. A detailed understanding of in-cylinder processes of the diesel fuel combustion is therefore important to maximize the benefits of dual-fuel combustion applications. Despite substantial progress in optical accessible CVCC, the most detailed available experiments can only provide a partial set of data under engine-like conditions. It is hence challenging to understand all the relevant combustion phenomena solely based on the experimental observation. For instance, the quantitative flame size can only be obtained at quasi-steady state. Effects of ρ_{am} and d_0 on

transient flame development can only be evaluated based on qualitative data and the data are scattered. Therefore, the use of computational fluid dynamic (CFD) and chemical kinetic mechanism models can help to shed more light onto the limited information from present experimental studies.

Various CFD works in the literature demonstrated the capability of the Transported Probability Density Function Model (TPDF) with a skeletal diesel surrogate model to simulate diesel spray flame. The effects of different $d_0^{(5)}$ and different ambient conditions, e.g. ρ_{am} , ambient temperature (T_{am}), and ambient oxygen levels ($O_{2,am}$)^(4,6,10), on diesel spray characteristics were investigated in numerous studies. However, there are only a few studies^(7,8,10) that compared the results (e.g. spray and flame characteristics) computed from the TPDF method and the Well-Stirred Reactor (WSR) model, where the latter model does not consider turbulence-chemistry interactions (TCI). In addition, these numerical studies were only carried out for small nozzle diameters ($\leq 100 \mu\text{m}$) and at low ambient density condition ($\rho_{am} < 30.0 \text{ kg/m}^3$). Both the d_0 and ρ_{am} are generally much larger for large two-stroke marine engines^(1,11-13).

Setting against this background, the current CFD work employs an Eulerian-based TPDF and WSR model with a skeletal n-heptane model to investigate the effects of d_0 and ρ_{am} on diesel spray combustion, in which ρ_{am} is used to represent different engine loads. At the same time, the influence of TCI on diesel spray and combustion characteristics is investigated by comparing the numerical results from the Eulerian-based TPDF and the WSR model. The paper is structured as follows. In Section 2, the description of model formulations is first shown, followed by the test cases and the operating conditions. Section 3 discusses the model validation based on optical measurements. This is followed by a detail numerical analysis of the TCI effect on the flame

structures under different operating conditions. Finally, concluding remarks from this work are then highlighted in Section 4.

2. NUMERICAL SETUP

2.1 Model formulation. The current three-dimensional (3-D) CFD spray combustion simulations are carried out using the open-source code, OpenFOAM-v1712⁽¹⁴⁾. The full numerical and geometrical setup have been reported in Ref. (17). For brevity, only key information are reported here. The skeletal n-heptane chemical kinetic mechanism developed by Liu *et al.*⁽¹⁹⁾ is employed as a diesel surrogate fuel model, while additional reactions are added for NO_x formation. For the operating conditions considered in the present study, thermal NO is expected to be the principal pathway for NO_x formation. Therefore, NO_x formation is modeled using the Zeldovich mechanism. The interaction between the turbulence and chemistry is modeled using an Eulerian-based TPDF, which is henceforth addressed as the Eulerian Stochastic Fields (ESF) method⁽²⁰⁾. The Well-Stirred Reactor (WSR) model, which has no turbulence-chemistry closure, is also considered in this study. The WSR model is not applicable for modeling thin reaction zones in flame propagation. In addition, there are also evidences that WSR tends to overpredict the lift-off length in the URANS modeling of spray combustion^(21,22). Despite this, the WSR model is still widely used to simulate compression-ignition combustion engines⁽²³⁻²⁶⁾. The chemistry-coordinate mapping (CCM) method is coupled with the ESF and WSR model in order to integrate the source terms due to chemical reactions more efficiently^(4,5,10). Full details pertaining to the CCM method are available in Ref. (10,27).

2.2 Case descriptions. The experiments from Sandia National Laboratory were chosen for numerical investigation in the current work. The experiments were conducted in an optical accessible CVCC under diesel engine-like conditions^(3,6,28-30). The initial ambient gas conditions

of the current test cases are listed in Table 1. Experimental data of diesel #2 is used in this work. The fuel is delivered at an injection pressure of 1400 bar through injectors with different d_0 . Since the injection pressure is fixed, the fuel mass flow rate from different nozzle increases with increasing d_0 . The measured IDT and lift-off length (LOL) are available in ECN database⁽²⁸⁾. Further information regarding the reacting spray cases are available in Refs. (3,6,28-30). The present investigation focuses on three d_0 of 100 μm , 180 μm , and 363 μm , as well as two levels of ρ_{am} at 30.0 kg/m^3 and 58.5 kg/m^3 . In order to clearly demonstrate the individual and the coupled effects of d_0 and ρ_{am} on spray and combustion characteristics, only one parameter (d_0 or ρ_{am}) is varied independently in each of the single factorial study while other parameters are fixed.

Table 1: Operating conditions and injection specifications in the current test cases.¹

| Case | $\text{O}_{2,am}$ | T_{am} [K] | ρ_{am} [kg/m^3] | d_0 [μm] | P_{inj} [bar] | \dot{m}_f [mg/ms] |
|------|-------------------|--------------|---------------------------------|-------------------------|-----------------|---------------------|
| 1 | 21% | 1000 | 30.0 | 100 | 1400 | 2.8 |
| 2 | 21% | 1000 | 30.0 | 180 | 1400 | 9.0 |
| 3 | 21% | 1000 | 30.0 | 363 | 1400 | 36.3 |
| 4** | 21% | 1000 | 58.5 | 100 | 1400 | 2.8 |
| 5 | 21% | 1000 | 58.5 | 180 | 1400 | 9.2 |
| 6** | 21% | 1000 | 58.5 | 363 | 1400 | 36.3 |

¹ $\text{O}_{2,am}$, T_{am} , ρ_{am} , d_0 , P_{inj} , and \dot{m}_f denote ambient oxygen levels, ambient gas temperature, ambient gas density, injection pressure, nozzle diameter, and fuel mass flow rate, respectively. (***) The \dot{m}_f for $\rho_{am} = 30.0 \text{ kg/m}^3$ case is used as no experimental \dot{m}_f is available for 58.5 kg/m^3 .

3. RESULTS AND DISCUSSION

3.1 Non-reacting spray characteristics. Model validation is first carried out on the sprays cases (Cases 1 – 6 in Table 1) at different ρ_{am} and d_0 values by performing inert spray simulations and computing their liquid penetration length (LPL) and vapor penetration length (VPL). It is important to note that $O_{2,am}$ is set to zero when performing inert spray simulations. The LPL is defined here as the maximum axial location from the injector encompassing 95 % of the total liquid mass, while the VPL is defined as the furthest axial distance with 0.1% mixture fraction.

Model evaluation of the liquid-phase is carried out by comparing against the LPL obtained from the liquid scaling law⁽³¹⁾ due to the lack of experimental measurements. The liquid properties of n-heptadecane are used in the liquid scaling law to produce diesel #2 liquid length⁽³¹⁾ since these resemble the properties of diesel #2. The computed LPL from different d_0 at ρ_{am} of 30.0 kg/m³ and 58.5 kg/m³ are depicted in Figure 1a. In the figure, the computed LPLs correspond well with the LPL obtained from the liquid scaling law across different ρ_{am} . On the other hand, the associated VPLs are evaluated by computing the dimensionless penetration length, σ and dimensionless penetration time, τ ,

$$\sigma = \frac{d_0 \sqrt{C_a} \sqrt{\rho_f / \rho_{am}}}{a \cdot \tan(\theta/2)} \quad (1)$$

$$\tau = \sigma \cdot \left(C_v \sqrt{\frac{2(P_{inj} - P_{am})}{\rho_f}} \right)^{-1} \quad (2)$$

where ρ_f and P_{am} denote the fuel density and ambient pressure, respectively. C_a and C_v refer to the orifice area-contraction coefficient and velocity coefficient, respectively. The spray dispersion angle is denoted as θ , while the term a is a constant. Full details of the methodology are available in Ref. (32). As seen in Figure 1b, all the σ curves collapse onto one another, which agrees with

the trend reported in Ref. (32). Overall, Figure 1 demonstrates that the model is successful in modeling the sensitivity of LPL and VPL to the change of d_0 and ρ_{am} .

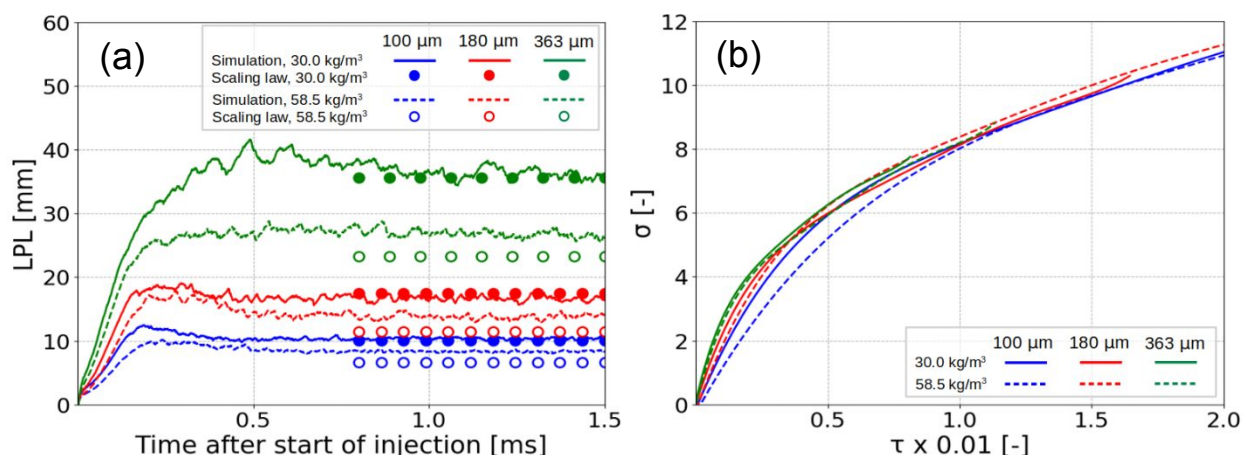


Figure 1: (a) Liquid penetration lengths (LPL) of non-reacting sprays as a function of time after start of injection. (b) Dimensionless penetration length (σ) as a function of dimensionless penetration time (τ) for different nozzle diameter and ambient density cases. Lines denote the simulations results. Circle markers denote the liquid scaling law results.

3.2 Ignition delay time and lift-off length. Figure 2 compares the simulated IDT and LOL with the experimental measurements. The IDT is defined as the time when the mixture is 400 K above its initial temperature, following the definition in Ref. (4). The LOL is defined as the shortest distance from the injector to the location with 2% of the maximum mass fraction of hydroxyl radical (OH)⁽²⁸⁾. At $\rho_{am} = 30.0 \text{ kg/m}^3$, the predicted IDTs using the ESF model for the nozzle diameters of 100 μm, 180 μm, and 363 μm have a relative difference of 47%, 6%, and 32%, respectively. Meanwhile, the predicted IDTs by the WSR model at 30.0 kg/m³ for all three nozzle diameters have a relative difference within 55%. On the other hand, the simulated IDTs by the ESF and WSR models under a higher ambient density condition ($\rho_{am} = 58.5 \text{ kg/m}^3$) have a relative difference within 30% as compared to experimental data. The discrepancies observed in the IDT

may likely be due to the experimental uncertainties from the hydraulic delay during fuel injection⁽³³⁾. Another possible reason could be due to the measured IDT being a pressure-based IDT, which is obtained from pressure measurements of a single pressure transducer. This pressure measurement requires adjustment to account for the time-delay in the measurement caused by the speed-of-sound, as well as the distance between the ignition site and the pressure transducer⁽³⁴⁾. Ignition sites were shown to vary differently across different nozzle sizes⁽¹⁷⁾. Meanwhile, luminosity images identifying the exact location of ignition were not acquired during the experiments of these three nozzles⁽³⁴⁾. Therefore, this may lead to uncertainties in the speed-of-sound time correction. Moreover, the use of a single pressure transducer may also lead to poor signal-to-noise ratio in pressure diagnostics⁽³⁵⁾. Based on Figure 2, it is worth mentioning that the influence of TCI on IDT is not obvious at both ambient densities of 30.0 kg/m³ and 58.5 kg/m³. This could be due to the shorter chemical timescale when under high ambient density conditions. This is, however, not the case for the LOL, where the ESF model predicts LOL that are consistently lower than the ones by the WSR model (cf. Figure 2). At the same time, the LOLs simulated using the ESF model correspond better with the measurements, with a maximum relative difference of 33% at both ambient densities. On the other hand, higher discrepancies are observed for the WSR predictions, where the relative differences to measurements are within 84% at both ambient densities. The present results for the 100 μm case is consistent with that by Bhattacharjee and Haworth⁽⁷⁾, where they compared the predicted IDT and LOLs using the Lagrangian-based TPDF and WSR models in their n-heptane spray flame simulations with $d_0 = 100 \mu\text{m}$. They suggested that as ρ_{am} (or P_{am} for a fixed T_{am}) increases, the chemistry becomes faster so that finite rate chemistry and TCI effects become relatively less prominent. The present work confirms the findings by Bhattacharjee and Haworth⁽⁷⁾ where it is shown here that the difference between the

predicted LOL between ESF and WSR reduces as ρ_{am} increases. This trend remains the same regardless of the d_0 used.

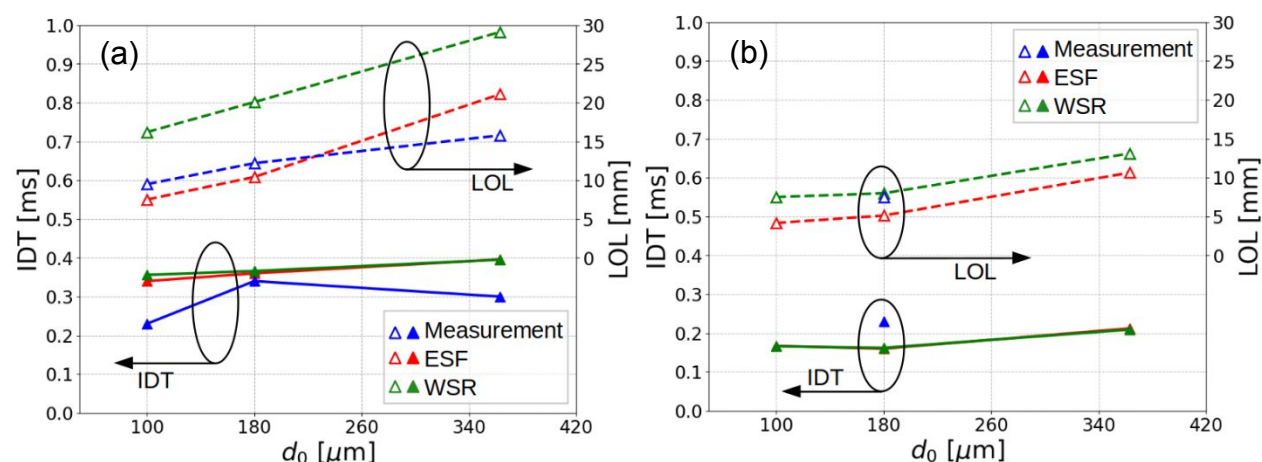


Figure 2: Ignition delay time (IDT) and lift-off length (LOL) for different nozzle diameters (d_0) predicted by the Eulerian Stochastic Fields (ESF) and Well-Stirred Reactor (WSR) models at (a) 30.0 kg/m³ (solid line, filled symbols) and (b) 58.5 kg/m³ (dashed line, open symbols) conditions.

3.3 Temporal evolution of vapor penetration, liquid penetration, and lift-off length. The cylinder bores of marine engines are larger as compared to those in automotive engines. This allows an established spray flame to form prior to flame-wall impingement⁽³⁶⁾. Vapor penetrations of the reacting sprays for different d_0 and ρ_{am} are shown in Figure 3. The vapor penetration of the associated non-reacting cases are also included to illustrate the increasing difference in time due to the combustion. Here, the reacting vapor penetration length is defined as the furthest axial position where 0.1% of mixture fraction is observed. The vapor penetration lengths are depicted in Figure 3 to increase with increasing d_0 at both ambient densities. In addition, minor differences can be observed in the predicted reacting vapor penetrations using ESF and WSR at both ambient densities of 30.0 kg/m³ (cf. Figure 3a) and 58.5 kg/m³ (cf. Figure 3b). The results imply that the

reacting vapor penetration is not significantly influenced by the TCI effect regardless of the ambient density conditions and nozzle diameters used.

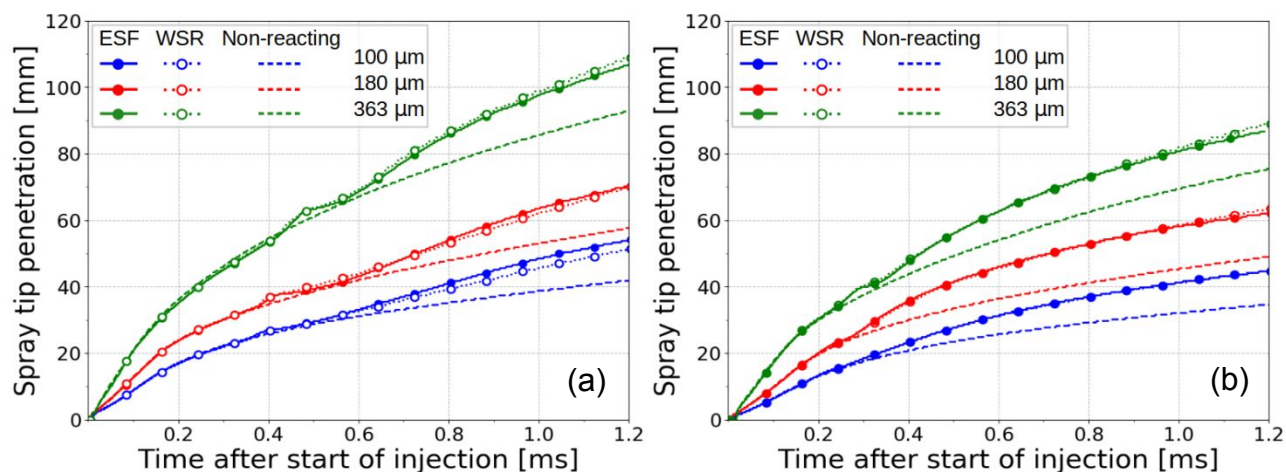


Figure 3: Comparisons of vapor penetration length for different nozzle diameters predicted by the Eulerian Stochastic Fields (ESF) and Well-Stirred Reactor (WSR) models under (a) 30.0 kg/m³ and (b) 58.5 kg/m³ conditions.

The temporal evolution of LPL and LOL for different nozzle diameters and TCI models is depicted in Figure 4. The LPLs predicted by both the ESF and WSR models are similar. Hence, only those predicted using the ESF model are shown in Figure 4.

At $\rho_{am} = 30.0 \text{ kg/m}^3$, the ignition sites predicted in the ESF cases are consistently closer to the injector than that predicted in the WSR cases (c.f. Figure 4a). The LOLs gradually shorten as the flames stabilize towards the injection tip when the ESF model is considered. On the other hand, the WSR model predicts flames that stabilize more quickly and at locations further downstream. In the 100 μm and 180 μm nozzle cases, the flame stabilization location leads to the LOL to be longer than the LPL in the WSR case, but vice-versa in the ESF case (cf. Figure 4a). This is, however, not similarly seen for the 363 μm nozzle case, where the LOLs predicted using the ESF

and WSR models are both shorter than the LPL (cf. Figure 4a). The implication of having longer LOL than LPL is later examined in Section 3.4.

At $\rho_{am} = 58.5 \text{ kg/m}^3$, the ignition sites predicted by the ESF and WSR models are closer to one another. Moreover, the LOL stabilizes more quickly than in the lower density case for both ESF and WSR models. The difference in the predicted LOL between the ESF and WSR models are now less obvious than that in the lower ambient density case ($\rho_{am} = 30.0 \text{ kg/m}^3$). In all the cases, the LOLs predicted by ESF and WSR models are consistently shorter than the associated LPL.

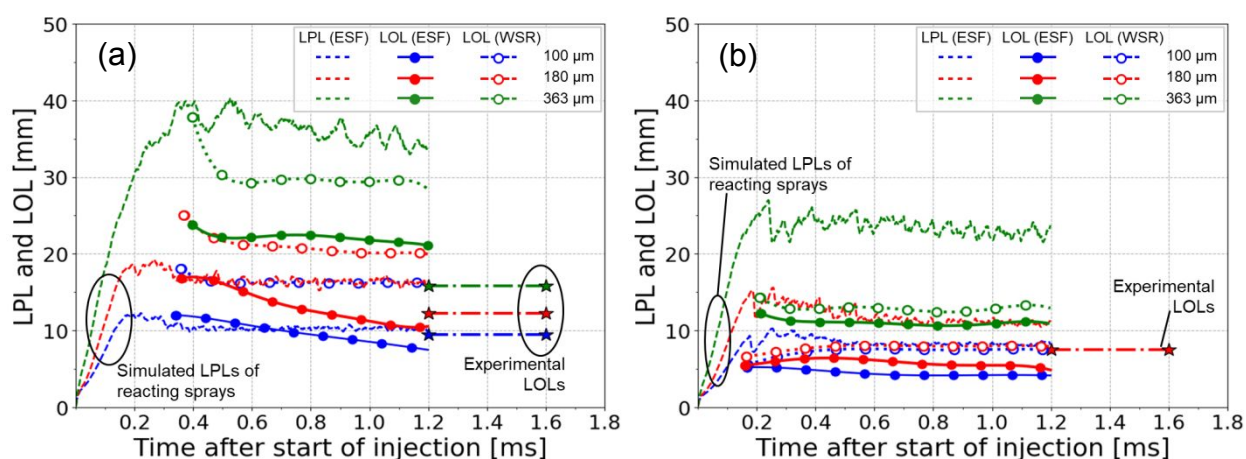


Figure 4: Temporal evolution of liquid penetration length (LPL) and lift-off length (LOL) predicted by the Eulerian Stochastic Fields (ESF) and Well-Stirred Reactor (WSR) models for different nozzle diameters under (a) 30.0 kg/m^3 and (b) 58.5 kg/m^3 conditions.

Based on Figure 4, it is shown that the ignition sites and the flame stabilization positions occur further downstream from the injection tip, which consequently lead to longer LOL, when d_0 increases. This is likely due to the longer liquid and vapor penetration lengths observed as d_0 increases. In order to take into account the influence of d_0 on the LOL and LPL, both the LOL and LPL are normalized by the equivalent diameter (d_{eq}) for each nozzle, i.e. $LOL^* = LOL/d_{eq}$ and $LPL^* = LPL/d_{eq}$, respectively. Following the same methodology in Ref. (37,38), the equivalent

diameter for each nozzle is computed as $d_{eq} = d_o \sqrt{\rho_f / \rho_{am}}$, where ρ_f denotes the density of fuel. The LPL* is depicted in Figure 5 to be insensitive to the variation of nozzle diameter for both ambient densities. This agrees with Sieber's empirical scaling law(31), which shows that $LPL \propto d_o \sqrt{\rho_f / \rho_{am}}$. The full description of the empirical scaling law can be seen in Ref. (31). Based on Figure 5, LOL* is shown to decrease with increasing d_o , which is opposite to the LOL trend observed in Figure 2. This observation suggests that the amount of fuel injected is more significant than the amount of air entrained, which may lead to a more fuel-rich mixture in the spray. The effect of LOL and LPL on fuel-air mixing is further investigated in the following section.

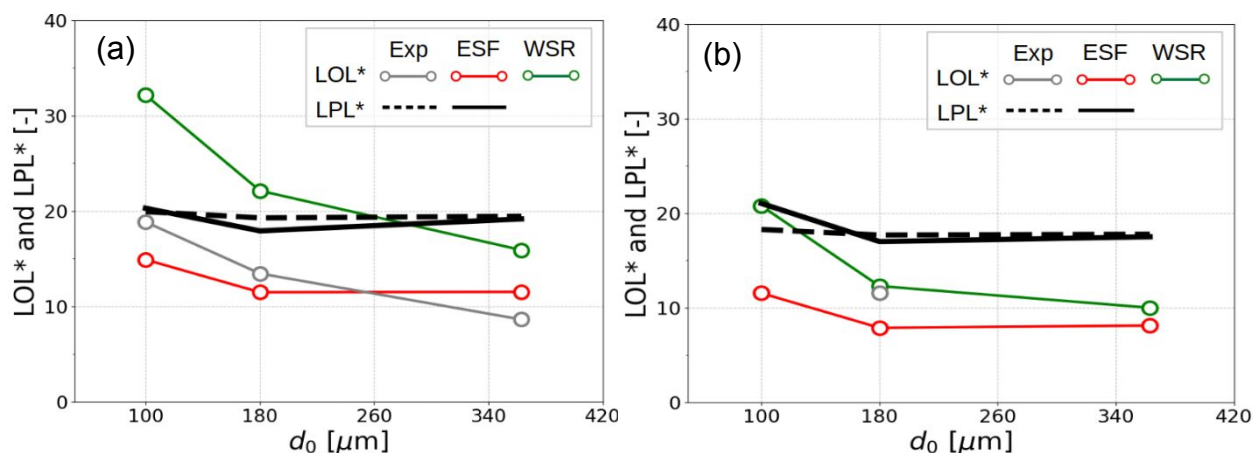


Figure 5: Normalized liquid penetration length (LPL*) and normalized lift-off length (LOL*) for different nozzle diameters using the Eulerian Stochastic Fields (ESF) and Well-Stirred Reactor (WSR) model under (a) 30.0 kg/m³ (solid lines, filled symbols) and (b) 58.5 kg/m³ (dashed lines, hollow symbols) conditions.

3.4 Temperature-equivalence ratio scatter plots. Figure 6 shows the scatter plots in the temperature-equivalence ratio ($T-\phi$) space for the spray flames during quasi-steady state. The rich premixed core region is defined here as the region where $\phi \geq 1.5$ and $1000 \text{ K} < T \leq 1600 \text{ K}$. Based on Figure 6, the rich premixed core region appears to vary with nozzle diameters and TCI model

used. The T - ϕ distribution predicted using the ESF model is different from that using the WSR model at an ambient density of 30.0 kg/m^3 (cf. Figure 6a and Figure 6c), whereas this difference is less apparent when at higher ambient density of 58.5 kg/m^3 (cf. Figure 6b and Figure 6d).

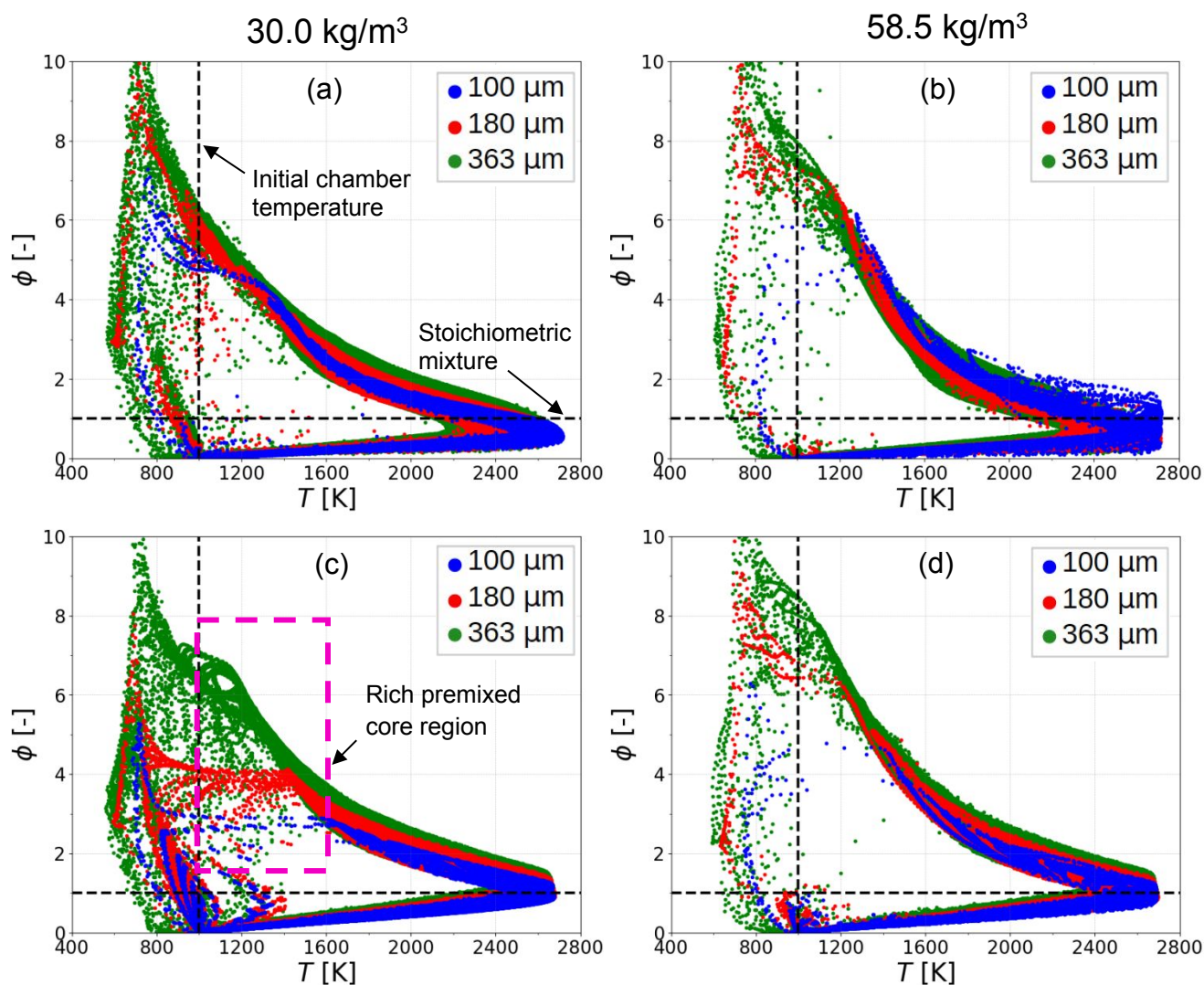


Figure 6: Comparisons of local temperature-equivalence ratio (T - ϕ) characteristics predicted using the Eulerian Stochastic Fields model (a-b) and Well-Stirred Reactor model (c-d) for different nozzle diameters under different ambient densities during quasi-steady state.

In order to better elucidate the effect of d_0 , ρ_{am} , and TCI model on the ϕ distribution in the rich premixed core region, the distribution of spray in the rich premixed core region is represented as a discrete probability density function (PDF) of ϕ and is depicted in Figure 7. The ϕ value within the rich premixed core region for a given d_0 usually decreases with the increase of LOL due to stronger air entrainment process. However, an opposite trend is observed in Figure 7, where the rich premixed core region becomes more fuel-rich as d_0 increases regardless of the TCI model and ρ_{am} considered. This is likely due to the larger amount of fuel being injected as d_0 increases (see Table 1). Furthermore, this also corresponds with the LOL* trend depicted in Figure 5, in which LOL* is shown to decrease as d_0 increases. The results imply that the amount of fuel injected is more significant than the amount of air entrained when d_0 increases. As a result, the premixed core region becomes more fuel-rich (cf. Figure 7). Based on the findings, it is suggested that LOL* is a better parameter to describe T- ϕ space for the spray flames obtained from different d_0 .

At ambient density of 30.0 kg/m³, it is notable from Figure 7a and Figure 7c that the premixed core region in the WSR case are significantly less fuel-rich than their ESF counterparts in the 100 μ m and 180 μ m nozzle cases. This is likely due to predicted LOL in the WSR case being longer than the LPL. Based on the work by Sieber and Higgins⁽²⁹⁾, the amount of air entrained into the flame was shown to be higher when the LOL is longer than the LPL. Meanwhile, based on Figure 4a and Figure 5a, the WSR model predicted LOL that are longer than the LPL in the 100 μ m and 180 μ m nozzle cases, but vice versa when the ESF model is used. As a result, the WSR cases with nozzle diameter of 100 μ m and 180 μ m experiences higher air entrainment, which eventually lead to less fuel-rich mixture in the premixed core region (cf. Figure 7c). In the large nozzle case (363 μ m), both the WSR and ESF models predicted LOL that are consistently shorter than the LPL (cf. Figure 4a and Figure 5a). This is similarly obtained across all three nozzle diameters when at a

higher ambient density of 58.5 kg/m^3 (cf. Figure 4b and Figure 5b). Therefore, it is shown that the difference in the PDF of ϕ between the ESF and WSR cases for these cases are relatively less apparent (cf. Figure 7). The above results demonstrate the importance of considering TCI effect for small nozzle cases and at low ambient density conditions to ensure an accurate prediction of the air entrainment process.

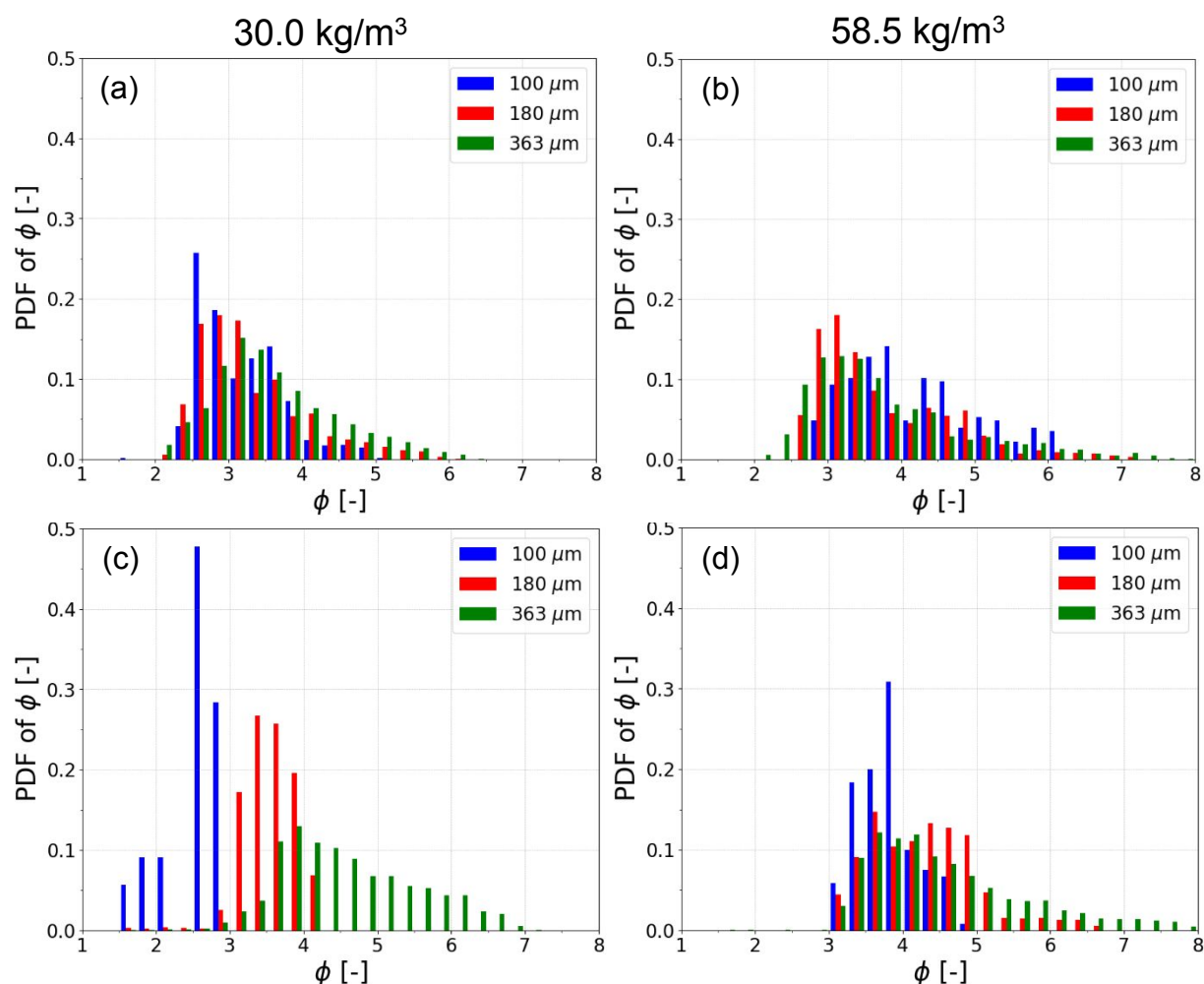


Figure 7: Discrete probability density function (PDF) of ϕ in the rich premixed core region for different nozzle diameters under different ambient densities during quasi-steady state using the Eulerian Stochastic Fields model (a-b) and Well-Stirred Reactor model (c-d).

3.5 Spatial distribution of intermediate species and emission. To understand the effects of the d_0 , ρ_{am} , and TCI model on the overall flame structure, the mass fractions of RO_2 , CH_2O , and OH are examined next. The heptyl peroxy radical ($\text{C}_7\text{H}_{15}\text{O}_2$, also known as RO_2) is one of the first species in the decomposition path of n-heptane and is therefore a good marker for the first-stage ignition and the low-temperature chemistry activity⁽³⁹⁾. Formaldehyde (CH_2O) is a product of the first-stage ignition which is frequently measured in experiments as a marker of regions where low-temperature (cool-flame) chemistry is underway^(40,41). Hydroxyl (OH) is selected as a marker of regions where high-temperature chemistry is active, also in accordance with several experimental studies^(35,42).

The spatial distributions of RO_2 mass fraction are shown in Figure 8. It is important to note that the peak RO_2 mass fraction in the ESF cases are consistently higher than that in the WSR cases regardless of d_0 and ρ_{am} considered (not shown). At $\rho_{am} = 30.0 \text{ kg/m}^3$, both WSR and ESF predicted RO_2 distribution that are similar to one another in the 100 μm and 180 μm cases (cf. Figure 8a and Figure 8b). However, when the d_0 increases to 363 μm , the RO_2 distribution predicted by the WSR model is significantly longer than that predicted by the ESF model (cf. Figure 8c). This inconsistency in the results is likely attributed to LOL being longer than LPL in the WSR cases with nozzle size of 100 μm and 180 μm . Due to longer LOL and stronger air entrainment process, the RO_2 distribution in the 100 μm and 180 μm cases is predicted to be shorter and further downstream from the injector. At $\rho_{am} = 58.5 \text{ kg/m}^3$, RO_2 distributions in the WSR and ESF cases correspond to one another across all three nozzle diameters. It likely due to smaller differences in the LOL predicted between WSR and ESF, as depicted in Figure 2. Therefore, it is suggested that RO_2 distribution becomes less sensitive to TCI effect as ambient density increases.

The spatial distribution of OH and CH₂O mass fraction at 1.2 ms using different TCI model and across different nozzle diameters are shown in Figure 9 ($\rho_{am} = 30.0 \text{ kg/m}^3$) and Figure 10 ($\rho_{am} = 58.5 \text{ kg/m}^3$). Based on Figure 9 and Figure 10, the CH₂O distribution are predicted differently by using ESF and WSR models. The CH₂O distribution in the ESF cases are generally longer axially and wider radially as compared to that in the WSR cases. Such results agree with that reported by numerous work^(43,44) at a lower ambient density of 14.8 kg/m^3 and nozzle diameter of $\leq 100 \text{ }\mu\text{m}$. Despite this, a noticeable difference can be seen in the $100 \text{ }\mu\text{m}$ and $180 \text{ }\mu\text{m}$ cases at $\rho_{am} = 30.0 \text{ kg/m}^3$ and the $100 \text{ }\mu\text{m}$ case at $\rho_{am} = 58.5 \text{ kg/m}^3$, where a significantly shorter span for the CH₂O distributions is predicted by the WSR model as compared to that by the ESF model. This observation is likely due to the difference in the rich premixed core region, as depicted in Figure 7. The fuel-rich premixed region in both the $100 \text{ }\mu\text{m}$ and $180 \text{ }\mu\text{m}$, WSR cases predicts relatively less fuel-rich mixture due to longer LOL. This subsequently led to a narrower and shorter mixture region for CH₂O to form. Focusing solely on the ESF cases, the axial span of the CH₂O distribution is shown to increase as the nozzle diameter increases at both ambient densities (cf. Figure 9a-c and Figure 10a-c). This is expected as the spray penetrates further downstream as nozzle diameter increases. Furthermore, it is worth highlighting that the predicted CH₂O distribution by the ESF model for the $363 \text{ }\mu\text{m}$ case corresponds well with its corresponding WSR counterpart at both ambient densities of 30.0 kg/m^3 (cf. Figure 9c and Figure 9f) and 58.5 kg/m^3 (cf. Figure 10c and Figure 10f). This observation may be attributed to both ESF and WSR models predicting similar mixture distribution in their rich premixed core region (cf. Figure 7). Hence, it is suggested that the effect of TCI on the CH₂O distribution becomes less significant when the nozzle diameter is large under the ambient conditions in the present study.

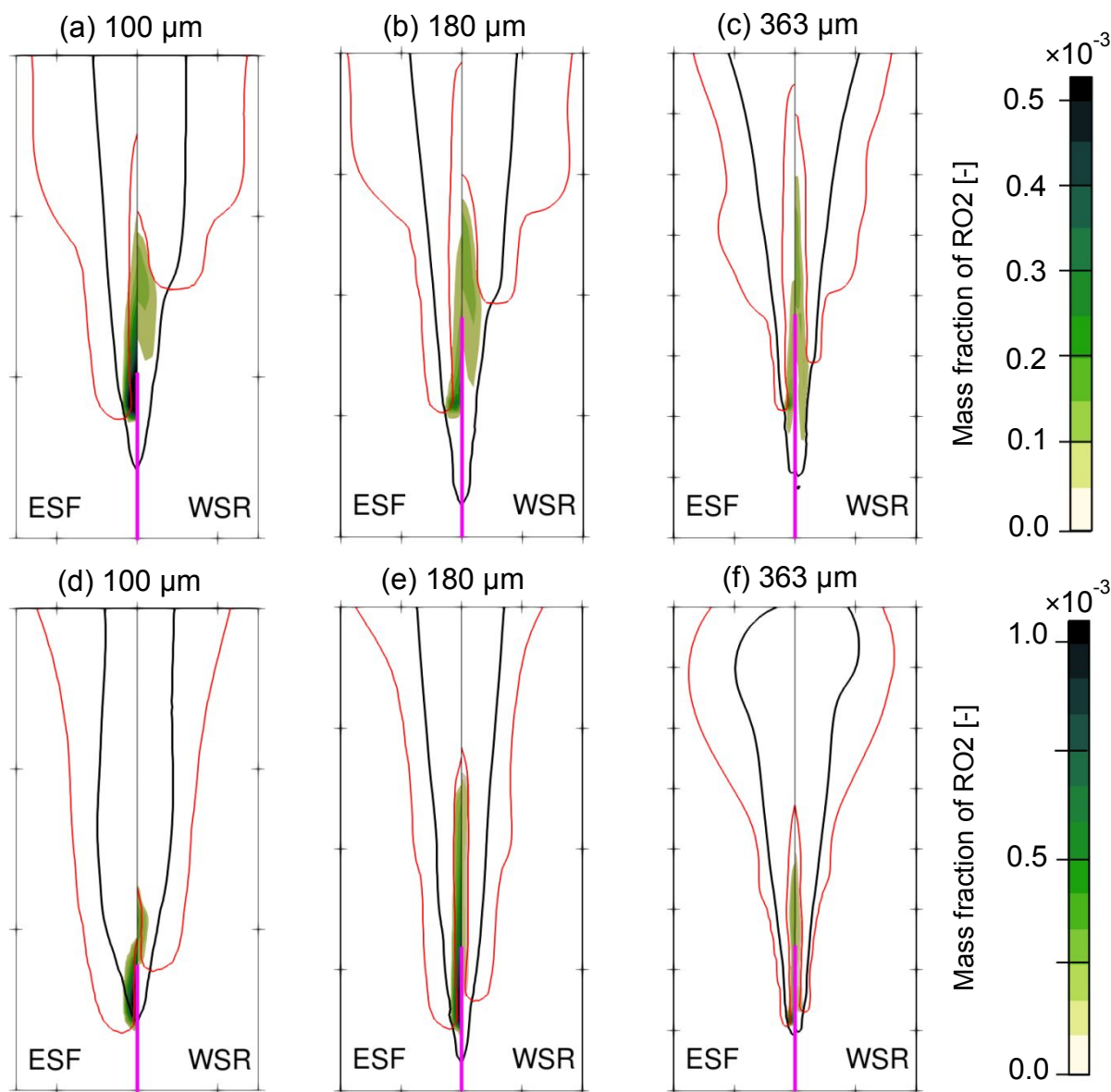


Figure 8: Mass fraction distribution of RO_2 at $t = 1.2$ ms by using the Eulerian Stochastic Fields (ESF) and Well-Stirred Reactor (WSR) model for different nozzle diameters under (a-b) 30.0 kg/m^3 and (d-e) 58.5 kg/m^3 conditions. Black solid lines represent the stoichiometric mixture fraction, Z_{st} . Solid magenta line represent averaged liquid length. Red solid represent iso-lines for temperature of 1200 K . Each frame for $100 \text{ }\mu\text{m}$, $180 \text{ }\mu\text{m}$, and $363 \text{ }\mu\text{m}$ shows $15 \times 30 \text{ mm}$, $20 \times 40 \text{ mm}$, and $40 \times 80 \text{ mm}$, respectively.

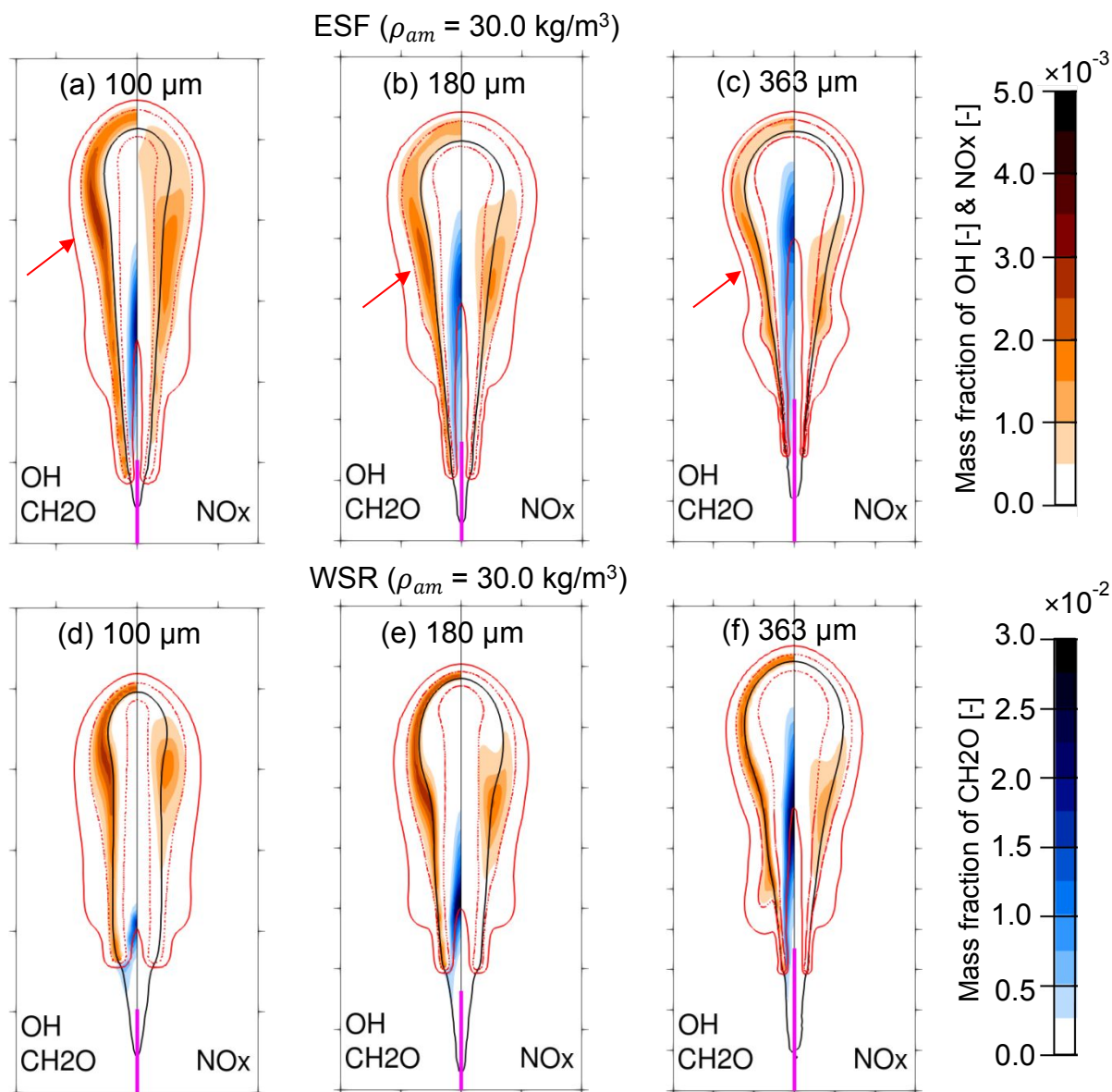


Figure 9: Mass fraction distribution of OH, CH₂O, and NO_x at $t = 1.2$ ms by using the Eulerian Stochastic Fields (a-c) and Well-Stirred Reactor (d-f) model for different nozzle diameters under 30.0 kg/m³ conditions. Black solid lines represent the stoichiometric mixture fraction, Z_{st} . Solid magenta line represent averaged liquid length. Red solid and dotted lines represent iso-lines for temperature of 1200 K and 2000 K, respectively. Each frame for 100 μm , 180 μm , and 363 μm shows 30 \times 60 mm, 40 \times 80 mm, and 60 \times 120 mm, respectively.

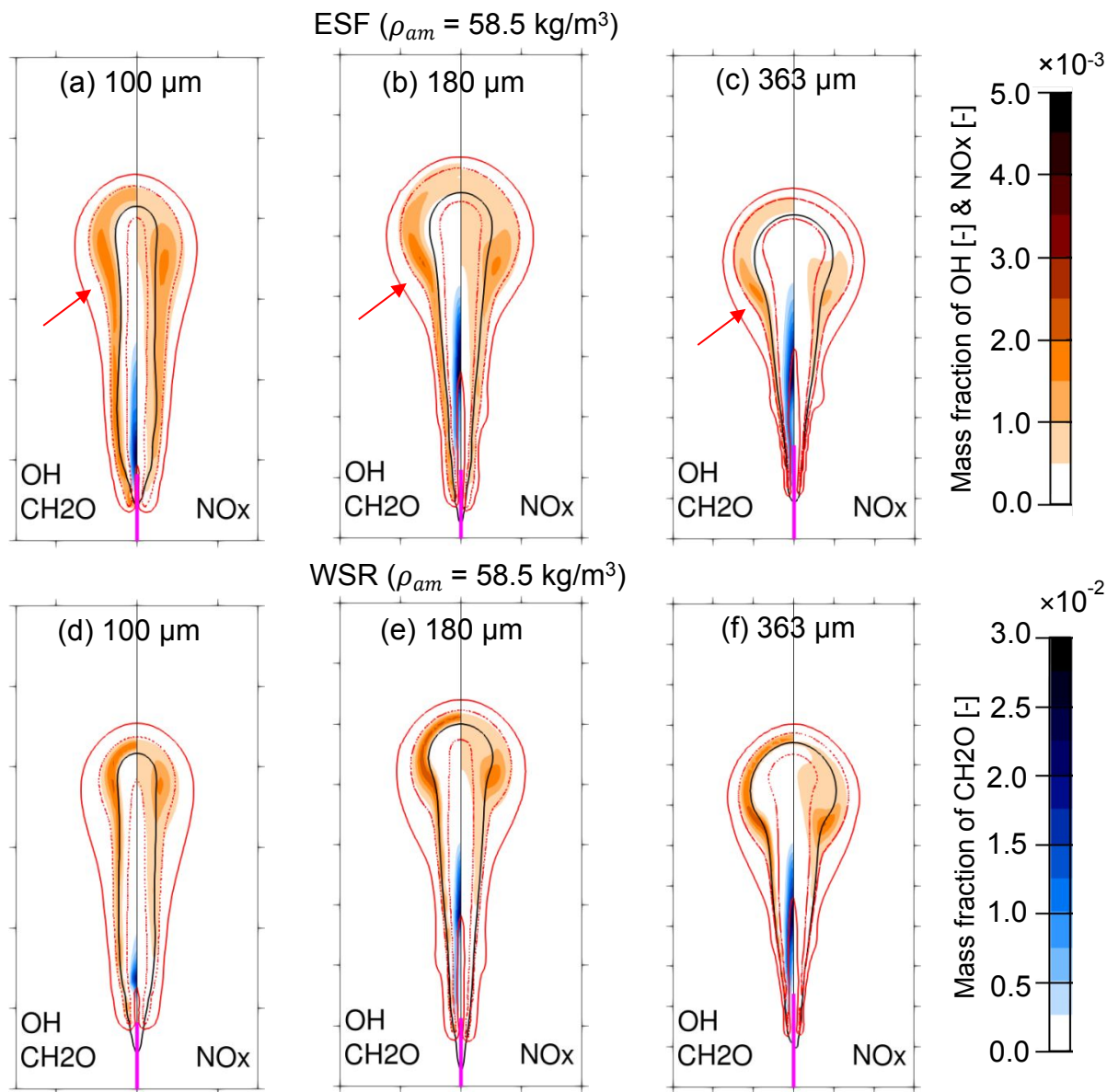


Figure 10: Mass fraction distribution of OH, CH₂O, and NO_x at $t = 1.2$ ms by using the Eulerian Stochastic Fields (a-c) and Well-Stirred Reactor (d-f) model for different nozzle diameters under 58.5 kg/m³ conditions. Descriptions can be found in the caption of Figure 9.

The OH distribution is examined next to better understand the effect of the ambient densities, nozzle diameter, and TCI model on high-temperature flame structure. At $\rho_{am} = 30$ kg/m³, the ESF results show a broader OH region, while the WSR model predicted a much thinner OH region for

all nozzle cases. Meanwhile, it is also notable that the peak OH regions are located differently between the ESF and WSR cases. In all the nozzle cases, high concentrations of OH are generally formed at the spray periphery in the ESF cases. This is indicated by red arrows in Figure 9a-c. In contrast, high concentrations of OH are formed at both the spray periphery and the spray head in the WSR cases (cf. Figure 9d-f). This difference in the distribution of OH can be similarly seen in the numerical results from Refs. (8,21) which uses different TCI model, e.g. TPDF and multiple representative interactive flamelet approaches. It is also obvious from Figure 9a-c that the effect of d_0 on the OH distribution varies between the ESF and WSR cases. The peak OH regions shrink more significantly in the ESF case as d_0 increases from 100 μm to 363 μm , while the region in the WSR case is rather insensitive to the variation of d_0 . It is worth noting that the aforementioned observations in the flame structure predicted by the ESF and WSR model at $\rho_{am} = 30.0 \text{ kg/m}^3$ are similarly captured when ambient density increases to 58.5 kg/m^3 , as depicted in Figure 10.

Figure 11 depicts the temporal evolution of maximum OH-mass fraction for different nozzle diameters at ambient densities of 30.0 kg/m^3 and 58.5 kg/m^3 . At $\rho_{am} = 30.0 \text{ kg/m}^3$, the maximum OH-mass fraction for the ESF cases are consistently lower than the ones predicted by the WSR model regardless of the nozzle diameter. This observation agrees with the findings in Refs. (7,8) which used the TPDF model. In contrast, the observation is not captured when ρ_{am} is increased to 58.5 kg/m^3 . At this high density condition, the computed maximum OH-mass fraction are shown to be insensitive to the effect of TCI model used as well as the variation of nozzle diameter size (cf. Figure 11b). This could be due to the extremely short chemical reaction time at high ambient density condition, thus rendering the TCI effect to be less significant to the ignition process.

The spatial distributions of NO_x computed using the WSR and ESF models are also depicted in Figure 9 and Figure 10 for different nozzle diameters and at different ambient densities. At $\rho_{am} =$

30.0 kg/m³, noticeable difference can be seen in when comparing the NO_x distribution by the WSR model to the one by ESF model in the small nozzle case ($d_0 = 100 \mu\text{m}$). This difference is, however, less apparent as d_0 increases to 363 μm . This is similarly observed at the higher ambient density condition of 58.5 kg/m³.

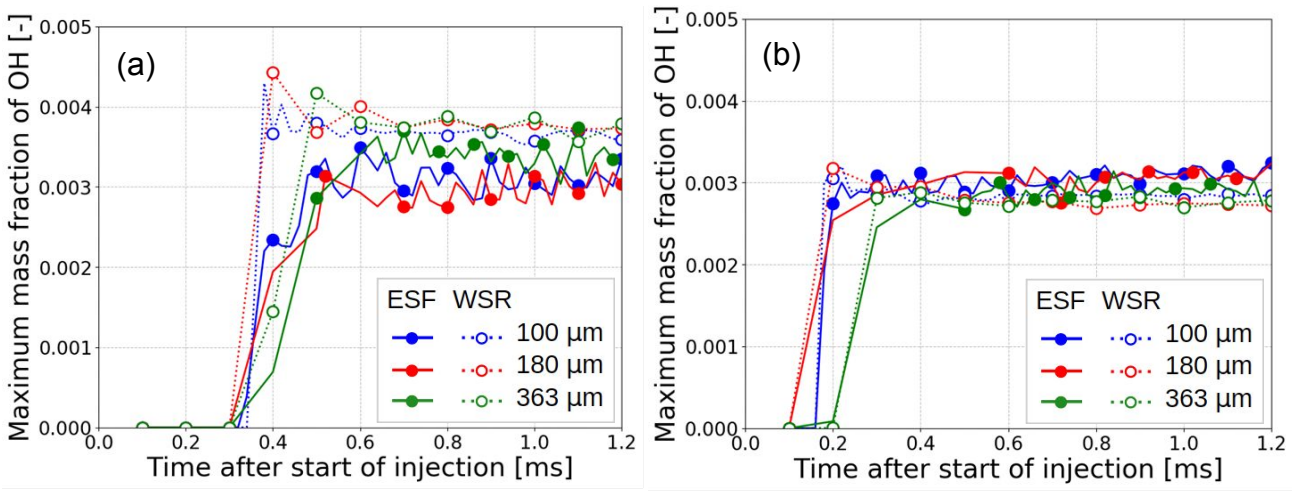


Figure 11: Maximum mass fraction of OH predicted by the Eulerian Stochastic Fields (ESF) and Well-Stirred Reactor (WSR) model for different nozzle diameters under (a) 30.0 kg/m³ and (b) 58.5 kg/m³ conditions.

Following the Zeldovich mechanism, NO_x formation strongly depends on the concentration of O and OH radicals⁽⁴⁵⁾. Therefore, it is obvious from Figure 9 and Figure 10 that the spatial location of the NO_x distributions in all the cases coincide with the spatial location of the high OH concentration. The same observation is obtained when examining the normalized mass of NO_x (Figure 12a-b) and OH (Figure 12c-d) for different nozzle diameters at different ambient densities using the ESF and WSR models. The predicted normalized NO_x mass are depicted to be akin to the temporal evolution of normalized OH mass. The predicted mass of NO_x formed are shown to decrease with increasing nozzle diameter at both ambient densities, regardless of TCI models used. This finding agrees with the simulation results in Refs. (46,47). Despite this, it is worth noting that

the difference in the predicted NO_x by using WSR and ESF model is also shown in Figure 12 to be the largest for the small nozzle case (100 μm), but smallest for the large nozzle case (363 μm). This observation provides supporting evidence that TCI effect on NO_x formation becomes less significant as d_0 increases.

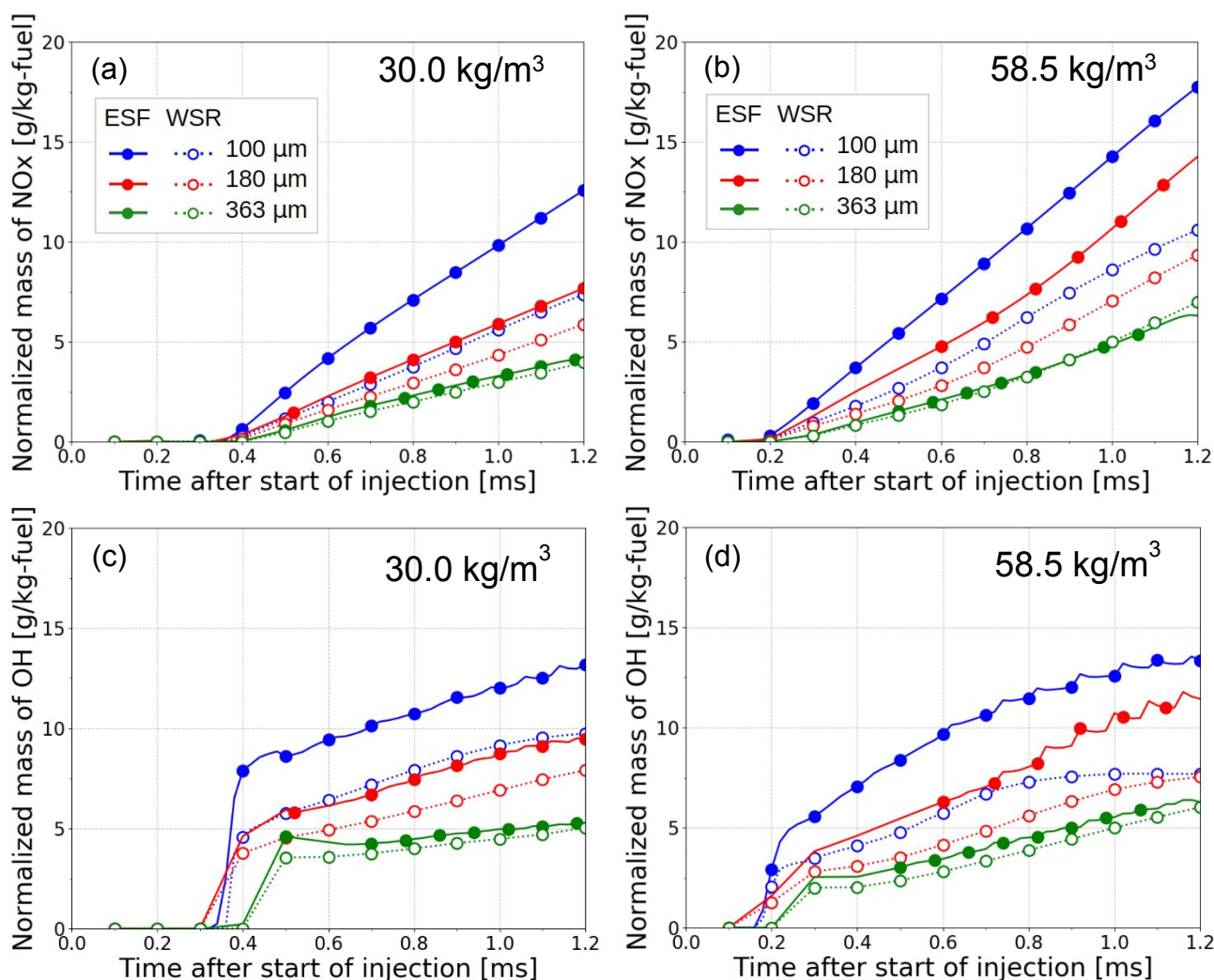


Figure 12: Normalized mass of NO_x (a-b) and normalized mass of OH (c-d) predicted by the Eulerian Stochastic Fields (ESF) and Well-Stirred Reactor (WSR) model for different nozzle diameters under 30.0 kg/m³ and 58.5 kg/m³ conditions.

4. CONCLUSIONS

The present work performs Unsteady Reynolds-averaged Navier-Stokes (URANS) simulations coupled with Eulerian Stochastic Fields (ESF) model and Well-Stirred Reactor (WSR) model to study the effect turbulence-chemistry interaction (TCI) on the spray and combustion characteristics of diesel spray under marine engine-like conditions. To replicate marine engine-like conditions, three nozzle diameters (d_0) of 100 μm , 180 μm , and 363 μm at two ambient gas densities (ρ_{am}) of 30.0 kg/m^3 and 58.5 kg/m^3 are considered in the current work.

A comparison to measurements shows that the ESF method can reproduce spray characteristics, ignition delay time (IDT), and lift-off length (LOL) with an improved accuracy than that from the WSR method. TCI has significant influence on LOL but not on IDT. A normalized LOL (LOL*) is introduced here, which considers the effect of d_0 on LOL, and its subsequent effect on the fuel-richness in the rich premixed core region is analyzed. In addition, insignificant differences is observed in the predicted vapor penetration lengths using the ESF and WSR models regardless of the nozzle diameters and ambient densities considered in the present study.

TCI effect on the spatial distribution of RO_2 becomes less significant as ambient density increases. The consideration of TCI closure causes notable effect on the spatial distribution of formaldehyde (CH_2O) and hydroxyl radical (OH). The ESF model generally predicts longer and wider CH_2O distribution as compared to that by the WSR model. The difference in the spatial distribution of CH_2O between the ESF and WSR model diminishes as d_0 increases to 363 μm . Meanwhile, the ESF model predicts a broader OH distribution than that by the WSR model at both ambient densities. However, the peak OH value in the ESF case is consistently lower than in the WSR case at 30.0 kg/m^3 , but are similar to one another at 58.5 kg/m^3 for all nozzle sizes. The total mass of OH formed in the ESF case is significantly more than that in the WSR case for $d_0 = 100$

1
2
3 μm at both ambient densities. However, the high concentration OH region is shown to shrink as
4
5 d_0 becomes larger. This consequently leads to the total mass of OH formed by the ESF and WSR
6
7 models to be close to one another in the large nozzle case. As NO_x forms from OH radicals, the
8
9 total NO_x mass formed follows qualitatively the total OH mass profile from different d_0 and ρ_{am}
10
11 using the ESF and WSR models.
12
13

14
15 In general, this URANS study clearly demonstrates that the effect of TCI on the global spray
16
17 and combustion characteristics becomes less prominent when d_0 increases.
18
19
20
21
22

23 AUTHOR INFORMATION

24 Corresponding Author

25
26
27
28 *Email: jcong@mek.dtu.dk
29
30

31 Notes

32
33 The authors declare no competing financial interest.
34
35
36
37
38

39 ACKNOWLEDGEMENT

40
41 The authors gratefully acknowledge the financial support from the Independent Research Fund
42
43 Denmark (DFF) and MAN Energy Solutions under the grant number 8022-00143B. The
44
45 computation was performed using the Niflheim cluster at the Technical University of Denmark
46
47 (DTU).
48
49
50
51
52
53
54
55
56
57
58
59
60

REFERENCES

1. Ishibashi R.; Tsuru D. An optical investigation of combustion process of a direct high-pressure injection of natural gas. *J Mar Sci Technol* **2016**;doi:10.1007/s00773-016-0422-x.
2. Pang KM.; Karvounis N.; Walther JH.; Schramm J.; Glarborg P.; Mayer S. Modelling of temporal and spatial evolution of sulphur oxides and sulphuric acid under large, two-stroke marine engine-like conditions using integrated CFD-chemical kinetics. *Appl Energy* **2017**;193:60-73.
3. Pickett LM.; Siebers DL. Orifice diameter effects on diesel fuel jet flame structure. *J Eng Gas Turbines Power* **2005**;127:187-96.
4. Pang KM.; Jangi M.; Bai X-S.; Schramm J.; Walther JH.; Glarborg P. Effects of ambient pressure on ignition and flame characteristics in diesel spray combustion. *Fuel* **2019**;237:676-85.
5. Pang KM.; Jangi M.; Bai X-S.; Schramm J.; Walther JH. Effects of Nozzle Diameter on Diesel Spray Flames: A numerical study using an Eulerian Stochastic Field Method. *Energy Procedia* **2017**;142:1028-33.
6. Pickett LM.; Siebers DL. An investigation of diesel soot formation processes using micro-orifices. *Proc Combust Inst* **2002**;29:655-62.
7. Bhattacharjee S.; Haworth DC. Simulations of transient n-heptane and n-dodecane spray flames under engine-relevant conditions using a transported PDF method. *Combust Flame* **2013**;160:2083-102.
8. Pei Y.; Hawkes ER.; Kook S. A comprehensive study of effects of mixing and chemical kinetic models on predictions of n-heptane jet ignitions with the PDF method. *Flow Turbul Combust* **2013**;91:249-80.

- 1
2
3 9. Pei Y,; Hawkes ER,; Kook S,; Goldin GM,; Lu T. Modelling *n*-dodecane spray and
4
5 combustion with the transported probability density function method. *Combust Flame*
6
7 **2015**;162:2006-19.
8
9
- 10 10. Pang KM,; Jangi M,; Bai X-S,; Schramm J,; Walther JH. Modelling of ignition and flame
11
12 liftoff using an accelerated Eulerian Stochastic Fields method. *Combust Flame* **2018**;193:363-
13
14 83.
15
16
- 17 11. Kyriakides N,; Chrysosakis C,; Kaiktsis L. Influence of heavy fuel properties on spray
18
19 atomization for marine diesel engine applications. No. 2009-01-1858. *SAE Technical Paper*,
20
21 **2009**.
22
23
- 24 12. Kilpinen, P. Optimization of a simplified sub-model for NO emission prediction by CFD in
25
26 large 4-stroke marine diesel engines. *Fuel Process. Technol*, **2010**, 91.2: 218-228.
27
28
- 29 13. Bolla M,; Srna A,; Wright YM,; Von Rotz B,; Herrmann K,; Boulouchos K. Influence of
30
31 injector diameter (0.2-1.2 mm range) on diesel spray combustion: measurements and CFD
32
33 simulations. No. 2014-01-1419. *SAE Technical Paper*, **2014**.
34
35
- 36 14. The OpenFOAM Foundation. **2017**. Available at < www.openfoam.org/ > [Accessed on 30
37
38 October 2020]
39
- 40 15. Lin R,; Tavlarides LL. Thermophysical properties needed for the development of the
41
42 supercritical diesel combustion technology: Evaluation of diesel fuel surrogate models. *J.*
43
44 *Supercrit Fluids* **2012**;71:136-46.
45
46
- 47 16. Reitz RD,; Diwakar R. Effect of drop breakup on fuel sprays. *SAE Paper* **1986**;860469.
48
- 49 17. Ong JC,; Walther JH,; Xu S,; Zhong S,; Bai XS,; Pang KM. Effects of ambient pressure and
50
51 nozzle diameter on ignition characteristics in diesel spray combustion.
52
53 *Fuel*.**2021**;290:119887.
54
55
56
57
58
59
60

18. Ranz WE,; Marshall WR. Evaporation from droplets, parts I & II. *Chem Eng Prog* **1952**;48:173-80.
19. Liu S,; Hewson JC,; Chen JH,; Pitsch H. Effects of strain rate on high-pressure nonpremixed n-heptane autoignition in counterflow, *Combust Flame* **2004**;137:320-39.
20. Valino L. A field Monte Carlo formulation for calculating the probability density function of a single scalar in a turbulent flow. *Flow, Turb Combust* **1998**;60:157-72.
21. D'Errico G,; Lucchini T,; Contino F,; Jangi M,; Bai XS. Comparison of well-mixed and multiple representative interactive flamelet approaches for diesel spray combustion modelling. *Combust. Theor. Model.*, **2014**, 18.1: 65-88.
22. Pang KM,; Jangi M,; Bai XS,; Schramm J,; Walther JH. Modelling of diesel spray flames under engine-like conditions using an accelerated Eulerian Stochastic Field method. *Combust. Flame*. **2018**;193:363-83.
23. Kokjohn SL,; Reitz RD. Reactivity controlled compression ignition and conventional diesel combustion: a comparison of methods to meet light-duty NOx and fuel economy targets. *Int. J. Eng. Res.* **2013**;14(5):452-68.
24. Abani N,; Reitz RD. Diesel engine emissions and combustion predictions using advanced mixing models applicable to fuel sprays. *Combust. Theor. Model.* **2010**;14(5):715-46.
25. Pang KM,; Karvounis N,; Walther JH, Schramm J, Glarborg P, Mayer S. Modelling of temporal and spatial evolution of sulphur oxides and sulphuric acid under large, two-stroke marine engine-like conditions using integrated CFD-chemical kinetics. *Appl Energy*. **2017**;193:60-73.

26. Karvounis N.; Pang KM.; Mayer S.; Walther JH. Numerical simulation of condensation of sulfuric acid and water in a large two-stroke marine diesel engine. *Appl energy*. **2018**;211:1009-20.
27. Jangi M.; Yu R.; Bai XS. Development of chemistry coordinate mapping approach for turbulent partially premixed combustion. *Flow Turbul Combust*, **2013**, 90.2: 285-299.
28. Engine Combustion Department of Sandia National Laboratories. Engine Combustion Network. Available at < <http://www.sandia.gov/ecn/> > [Accessed on 26 October 2020]
29. Siebers D.; Higgins B. Flame lift-off on direct-injection diesel sprays under quiescent conditions. *SAE Paper* **2001**;2001-01-0530.
30. Pickett LM.; Siebers DL. Soot in diesel fuel jets: effects of ambient temperature, ambient density, and injection pressure. *Combust Flame* **2004**;138:114-35.
31. Siebers DL. Scaling liquid-phase fuel penetration in diesel sprays based on mixing-limited vaporization. *SAE transactions*, **1999**, 703-728.
32. Naber JD.; Siebers DL. Effects of gas density and vaporization on penetration and dispersion of diesel sprays. *SAE Paper* **1996**;960034.
33. Manin J.; Bardi M.; Pickett LM.; Payri R. Boundary condition and fuel composition effects on injection processes of high-pressure sprays at the microscopic level. *Int. J. Multiph. Flow*, **2016**, 83: 267-278.
34. Higgins B.; Siebers D.; Aradi A. Diesel-spray ignition and premixed-burn behavior. *SAE transactions*. **2000**, 1:961-84.
35. Lillo PM.; Pickett LM.; Persson H.; Andersson O.; Kook S. Diesel spray ignition detection and spatial/temporal correction. *SAE Int. J. Engines*. **2012**;5(3):1330-46.

- 1
2
3 36. Hult J,; Matamis A,; Baudoin E,; Mayer S,; Richter M. Spatiotemporal flame mapping in a
4 large-bore marine diesel engine using multiple high-speed cameras. *Int. J. Eng. Res.*
5 **2020**;21(4):622-31.
6
7
8
9
10 37. Pastor JV,; Garcia-Oliver JM,; Garcia A,; López AM. An experimental investigation on spray
11 mixing and combustion characteristics for spray C/D nozzles in a constant pressure vessel.
12 No. 2018-01-1783. *SAE Technical Paper*, **2018**.
13
14
15
16
17 38. Desantes JM,; Garcia-Oliver JM,; Novella R,; Pachano L. A numerical study of the effect of
18 nozzle diameter on diesel combustion ignition and flame stabilization. *Int. J. Eng. Res.*, **2020**,
19 21.1: 101-121.
20
21
22
23
24 39. Westbrook CK. Chemical kinetics of hydrocarbon ignition in practical combustion systems
25
26
27 *Proc Combust Inst.* **2000**, 1;28(2):1563-77.
28
29
30
31
32 40. Skeen S,; Manin J,; Pickett LM. Visualization of ignition processes in high-pressure sprays
33 with multiple injections of n-dodecane. *SAE Int. J. Engines.* **2015**;8(2):696-715.
34
35
36 41. Skeen SA,; Manin J,; Pickett LM. Simultaneous formaldehyde PLIF and high-speed schlieren
37 imaging for ignition visualization in high-pressure spray flames. *Proc. Combust. Inst.*
38 **2015**;35(3):3167-74.
39
40
41
42
43 42. Pickett LM,; Genzale CL,; Bruneaux G,; Malbec LM,; Hermant L,; Christiansen C,; Schramm
44 J. Comparison of diesel spray combustion in different high-temperature, high-pressure
45 facilities. *SAE Int. J. Engines.* **2010**;3(2):156-81.
46
47
48
49
50 43. Bolla M,; Farrace D,; Wright YM,; Boulouchos K,; Mastorakos E. Influence of turbulence–
51 chemistry interaction for n-heptane spray combustion under diesel engine conditions with
52 emphasis on soot formation and oxidation. *Combust. Theor. Model.* **2014**;18(2):330-60.
53
54
55
56
57
58
59
60

- 1
2
3 44. Lehtiniemi H.; Borg A.; Mauss F. Combustion modeling of diesel sprays. *SAE Technical*
4
5 *Paper*; **2016**; 2016-01-0592.
6
7
8 45. Turns SR. Introduction to combustion: concepts and applications, 3rd ed., *McGraw-Hill*
9 *international Edition, New York*, **2012**. Chapter 15, Pollutant Emissions; p. 559-560.
10
11
12 46. Zhang L.; He Z.; Wang Q.; Guo G. Effect of nozzle hole size coupling with exhaust gas re-
13
14 circulation on the engine emission performance based on KH-ACT spray model. *Therm. Sci.*,
15
16 **2015**, 19.6: 2003-2012.
17
18
19 47. Dunin AY.; Quynh NT.; Shatrov MG.; Golubkov LN. Analysis of the nozzle hole diameter
20
21 effect to common rail diesel engine characteristics using a calculated model of an internal
22
23 combustion Engine. *International Journal*, **2020**, 8.6.
24
25
26
27
28
29
30
31
32
33
34
35
36
37
38
39
40
41
42
43
44
45
46
47
48
49
50
51
52
53
54
55
56
57
58
59
60

TOC Graphics

